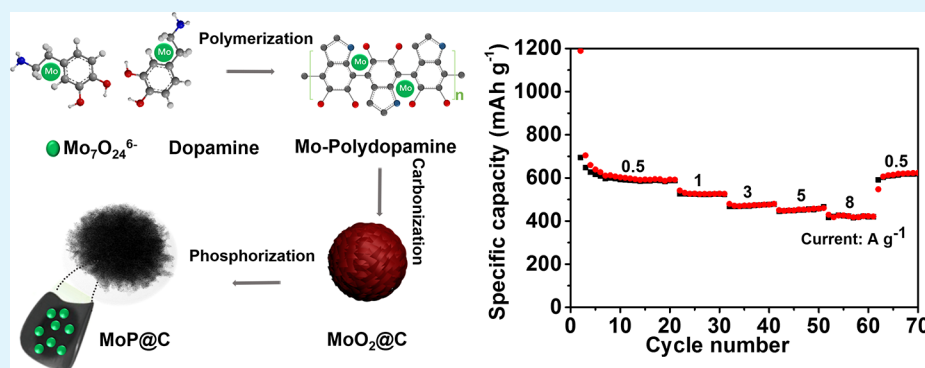


Urchin-like MoP Nanocrystals Embedded in N-Doped Carbon as High Rate Lithium Ion Battery Anode

Chunrong Ma,[†] Changjian Deng,[‡] XiaoZhen Liao,^{*,†} YuShi He,[†] ZiFeng Ma,^{†,§} and Hui Xiong^{*,‡,§}[†]School of Chemistry and Chemical Engineering, Shanghai Jiao Tong University, Shanghai, 200240, China[‡]Micron School of Materials Science and Engineering, Boise State University, Boise, Idaho 83725, United States[§]Sinopoly Battery Research Centre, Shanghai, 200241, China

S Supporting Information



ABSTRACT: Transition metal phosphides (TMPs) have gained extensive attention as an attractive candidate for anode materials used in lithium-ion batteries owing to their relatively low potentials and high theoretical capacities. Nevertheless, TMPs suffer from severe volume changes during cycling and low electrical conductivity, which limit their further applications. To achieve high energy and power density, constructing carbon/transition metal phosphide nanostructures is one of the most effective approaches because of enhanced electron/ion transport. Herein, we report urchin-like spheres assembled by MoP nanoparticles uniformly embedded in ultrathin carbon sheets via a template-free method. The unique structure of the spheres offers a synergistic effect to accommodate the mechanical stress during cycling, inhibit nanoparticles aggregation, and facilitate charge transfer during lithiation/delithiation processes. As a proof of concept, the nanocomposite electrode exhibits outstanding cycling stability at a high current rate (e.g., no obvious capacity decay after 400 cycles at 3 A g⁻¹) and superior rate performance (e.g., 415 mAh g⁻¹ at 8 A g⁻¹).

KEYWORDS: transition metal phosphide, anode, high rate, nanoarchitecture, lithium ion batteries

1. INTRODUCTION

Rechargeable lithium ion batteries (LIBs) are studied extensively and utilized for electric vehicles (EV) and portable electronics,^{1–4} since they were first commercialized by Sony. Growing consumer demands have stimulated great interests in developing low-cost electrode materials with long cycling stability and high energy and power densities. As an alternative to conventional anodes, conversion-type anode materials, such as oxides,^{5–8} fluorides,^{9–11} sulfides,^{12–14} and phosphides,^{15–20} have drawn great attention as advanced anode materials for LIBs owing to their superior volumetric and gravimetric capacities. Among them, metal phosphides stand out because of relatively low operation potentials and low polarization.^{21–23} However, poor cycling stability as a result of dramatic volume change during the charge/discharge processes is the major challenge for practical applications. To address these issues, nanostructuring presents an effective approach,^{6,14,15,18} which is advantageous because of shortened solid-state diffusion paths for fast kinetics. Nanostructured metal phosphide

anodes, such as nanoparticles,¹⁵ nanosheets,²¹ nanorods,^{24,25} nanowires,²⁶ and hollow spheres,¹⁷ have been reported. Although their electrochemical charge storage properties have been improved, to a certain extent, achieving long cycle life with superior rate capability still remains a challenge.

Molybdenum phosphides (MoP) have shown good electrochemical activity and high catalytic properties as catalysts for hydrogen evolution reaction.^{27–30} However, the application of MoP in LIBs is scarcely investigated. MoP is a conversion-type electrode material possessing theoretical specific capacity of 632 mAh g⁻¹, as well as a moderate operation potential and ecofriendliness. Despite of the advantages, MoP is still suffering from problems, such as low electrical conductivity, large volume expansion, and sluggish ion transport. Cho et al.³¹ reported MoP₂ anode synthesized by a mechanochemical

Received: September 17, 2018

Accepted: November 26, 2018

Published: November 26, 2018

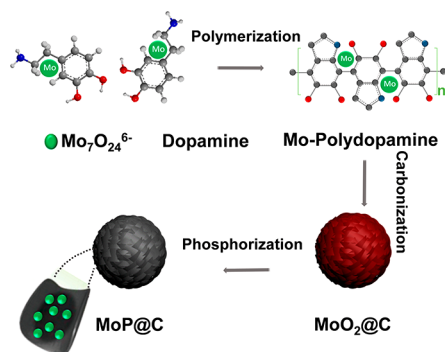
method, which has shown a capacity of 500 mAh g⁻¹ at a 0.2 C rate but for only 60 cycles. It still remains a challenge for molybdenum phosphide anode materials to realize their practical potential for extended cycling for LIBs. To tackle these problems, constructing a doped-carbon incorporated nanocomposite with strong coupling between active nanoparticles and carbonaceous materials could be an effective way. The doped-carbon matrix could not only serve as a barrier to prevent aggregation of nanoparticles, but also improve the electrical conductivity and shorten the electron transport path to realize a superior Li-storage performance. In particular, a uniquely architected nanoelectrode with high active surface area can be useful to promote the penetration of the electrolyte and alleviate volume expansion during cycling, ensuring stability of structures.

Herein, we demonstrate an urchin-like MoP nanocrystal embedded in the N-doped carbon matrix (MoP@C) through a self-polymerization of dopamine hydrochloride followed by a phosphidation process. In the synthesis, dopamine hydrochloride is used to control the particle shape and to serve as the carbon source for the hierarchical MoP@C. Of particular interest, the obtained structure is quite unique from previous reported metal-carbon composites.^{18,21,32,33} The designed nanoarchitecture presents several benefits: (1) the size of MoP nanocrystals is confined at nanoscale from aggregation by the polymerization of dopamine, which can be very useful to shorten the Li⁺ diffusion paths and increase the contact area; (2) the homogeneously dispersed MoP nanocrystals in the carbon matrix through the mixing of Mo precursor and dopamine solutions could increase the contact area between the active material and carbon matrix, and then decrease the average stress resulted from Li⁺ insertion/extraction to promote the structural stability upon extended cycling; (3) the interconnected conductive paths formed by the carbonation of polydopamine favor fast electron transport, enhancing rate capability. Consequently, the MoP@C electrode exhibits excellent lithium storage performance in terms of cycling stability and rate capability.

2. RESULTS AND DISCUSSION

As illustrated in Scheme 1, the synthesis of urchin-like MoP@C include the following procedures. First, the Mo-polydopamine composite was prepared via self-polymerization of dopamine with Mo₇O₂₄⁶⁻ under alkaline condition. Second, the well-defined MoO₂ nanocrystal embedded in the carbon composites (MoO₂@C) were produced by heating Mo-

Scheme 1. Schematic Illustration for the Preparation of MoP@C



polydopamine (Mo-PDA) precursor. After the phosphorization treatment, the MoO₂@C was transformed into MoP@C. The morphology and structure of the MoP@C were investigated by scanning electron microscopy (SEM) and transmission electron microscopy (TEM). As shown in Figure 1a, it is observed that the MoP@C has an urchin-shaped

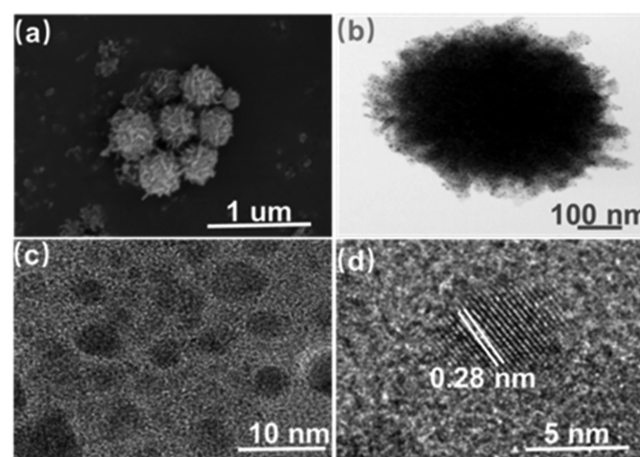


Figure 1. (a) SEM, (b) low-magnification TEM, and (c and d) high-magnification TEM images of the as-prepared MoP@C.

structure made of carbon nanosheets. This structure was further characterized by TEM (Figure 1b), showing an urchin-like structure with an average diameter of ~500 nm composed of well-defined nanoparticles, which is consistent with the MoO₂@C (Figure S1). The high magnification TEM image (Figure 1c) clearly demonstrates that MoP nanocrystals (~5 nm) are embedded throughout the carbon sheets uniformly, which can prevent erosion of MoP by electrolyte and ensure interfacial and structural stability of the active materials. The high-resolution TEM (HRTEM) (Figure 1d) shows lattice fringes with a 0.28 nm spacing, which is corresponding to the (100) planes of MoP (JCPDS card no. 65-6487). In addition, the elemental composition and distribution of MoP@C were examined by elemental mapping. It is confirmed that the distribution of Mo, P, C, and N elements is uniform throughout the whole sample (Figure S2). To reveal the role of dopamine during the synthesis of the urchin-like MoP@C, control MoP particles were also prepared using the same method without dopamine, which only led to large aggregates of solid MoP particles (Figure S3). It is evident that the polymerization of dopamine molecules as well as MoP particle growth can be affected by the reaction of metal chelation through formation of Mo-PDA.³⁴

XRD result shown in Figure 2 demonstrates that the as-prepared MoP adopts the hexagonal structure (JCPDS card no. 65-6487) without any other phase. Additionally, the size of MoP nanoparticle is determined to be ~4.2 nm according to the Scherrer equation,³⁵ which agrees well with the TEM results. A nitrogen adsorption-desorption measurement was performed to examine the porous structure. As shown in Figure 2b, a typical IV isotherm is observed, indicating that the presence of abundant mesopores in the nanocomposite.³⁶ According to the nitrogen adsorption-desorption isotherm, MoP@C exhibits a BET surface area of 185 m² g⁻¹.

Raman spectroscopy is performed to investigate the structure of the nanocomposite. There are two distinct peaks (Figure 2c) located at 1348 and 1590 cm⁻¹, which can be

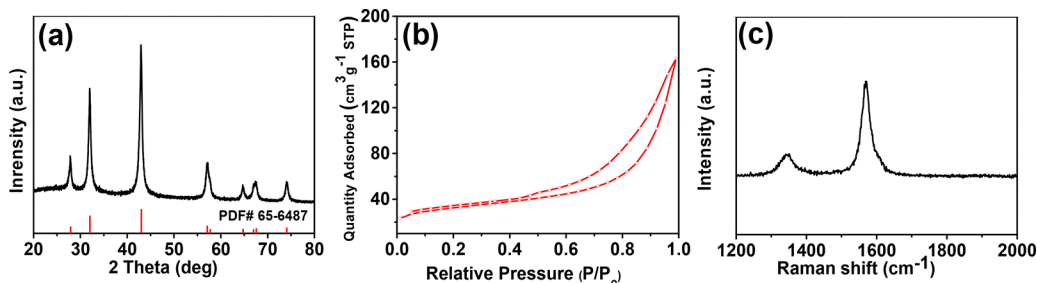


Figure 2. (a) XRD pattern of MoP@C, (b) the N_2 adsorption isotherms of the as-prepared MoP@C, and (c) the Raman spectrum of the MoP@C.

assigned to the D (disordered sp^2 carbon) and G band (graphitic sp^2 carbon) of carbon materials, respectively. The I_D/I_G is 0.54, demonstrating the existence of graphitic carbon. The active material content in the MoP@C composite is studied using thermogravimetric analysis (TGA). From Figure S3, during heat treatment, a small weight loss below 280 °C can be explained by the water removal. Above 280 °C, the distinct weight loss until 700 °C is ascribed to the carbon combustion accompanied by the oxidation of MoP. The final content of MoP and carbon in the MoP@C composite is determined to be 51% and 49%, respectively.

The chemical state of the urchin-like MoP@C sample is investigated by X-ray photoelectron spectroscopy (XPS). The survey spectrum (Figure S5) presents the characteristic peaks of Mo, P, C, and N. Mo 3d spectrum is shown in Figure 3a, the

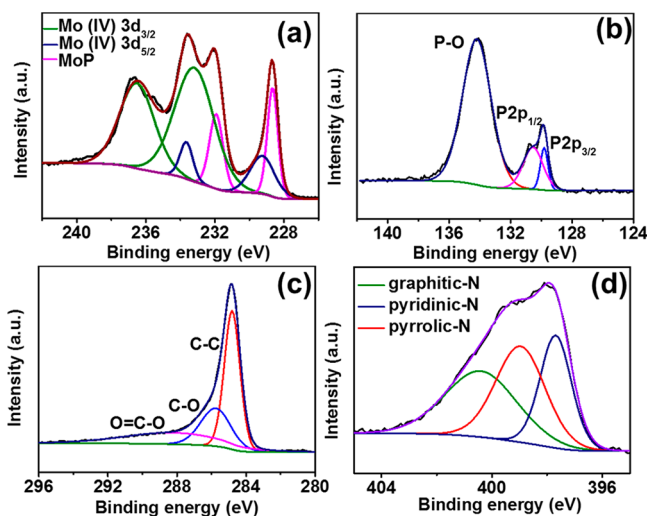


Figure 3. High-resolution XPS spectrum of (a) Mo 3d, (b) P 2p, (c) C 1s, and (d) N 1s of the MoP@C.

peaks at 236.4 and 233.4 eV correspond to the Mo (II) ($3d_{3/2}$) and Mo ($3d_{5/2}$) peaks. Two peaks presented at 231.5 and 229.1 eV can be attributed to the Mo (IV) $3d_{3/2}$ and $3d_{5/2}$ peaks from MoO_3 , due to the weak surface oxidation of molybdenum phosphide when exposed to air.³⁷ The other two peaks located at 232.3 and 228.2 eV are assigned to MoP, which is consistent with previous report.²⁹ The high resolution P 2p spectrum is shown in Figure 3b. There is a distinct peak with a binding energy of 134 eV, which corresponds to the P–O. Meanwhile, the peaks at 128.9 and 131.0 eV could be explained to the P $2p_{3/2}$ and P $2p_{1/2}$ of MoP. Additionally, the high-resolution C 1s spectrum is fitted to three peaks: the prominent peak at 285.9 eV corresponds to graphitic C, whereas the other two peaks located at 285.8 and 288.7 eV, are

attributed to the C–O and O=C=O, respectively. The N 1s spectrum is shown in Figure 3d, where three nitrogen species are identified: pyridinic-N, graphitic-N, and graphitic-N with binding energy of 397.6, 399.2, and 400.9 eV, respectively.³⁸ According to previous reports,^{39,40} the nitrogen-doping can offer superior electronic conductivity and more active sites, promoting fast reaction kinetics of lithium storage.

The electrochemical performance of the urchin-like MoP@C composite were investigated using Li half-cells. The galvanostatic discharge–discharge voltage profiles are shown in Figure 4a. MoP@C electrode exhibits an initial discharge capacity of 1080 $mAhg^{-1}$ and charge capacity 621 $mAhg^{-1}$, with a corresponding Columbic efficiency (CE) of 58%. The relatively low initial CE is still a challenge for almost all alloy or conversion type anodes (e.g., Si, sulfides, fluorides, oxides, and phosphides), which is associated with the solid electrolyte interphase (SEI) film formation.^{33,41,42} After several cycles, the CE is up to ~99.8%, which can be attributed to the uniform distribution of MoP nanocrystals into the N-doped carbon matrix, preventing MoP from further reactions with the electrolyte. It is worth noting that beyond the first cycle, the discharge and charge profiles almost overlap for subsequent cycles, indicating a superior cycling stability after the activation in the first cycle.

The rate capability of the urchin-like MoP@C is evaluated (Figure 4b). The MoP@C electrode delivers the specific discharge capacities of 602, 525, 475, and 450 $mAh g^{-1}$ at the current rates of 0.5, 1, 3, and 5 $A g^{-1}$. Impressively, a discharge capacity of 415 $mAh g^{-1}$ is achieved even at a high current rate of 8 $A g^{-1}$. Moreover, after deep cycling at high current densities, the electrode still recovers to a discharge capacity of 600 $mAh g^{-1}$ when the current rate is set back to 0.5A g^{-1} . This superior rate performance indicates that the as-prepared urchin-like MoP@C composite could accommodate high rate cycling without collapse of the structure, favoring the fast Li^+ and electron transport. In addition, the cycle life of the urchin-like MoP@C electrode is evaluated (Figure 4c). A reversible capacity of 496 $mAh g^{-1}$ is maintained without obvious decay and slightly increases from the initial capacity of 412 $mAh g^{-1}$, which can be attributed to the increased accesses to electrolyte after the lithiation/delithiation process.^{43,44} The long cycling performance of the as-prepared MoP@C composite electrode is assessed at a high current rate of 8 $A g^{-1}$. From Figure S5, the electrode maintains a specific capacity of 400 $mAh g^{-1}$ after 1000 cycles, suggesting the high reversibility and structure stability of MoP@C composite electrode. The cycled electrode was also evaluated by TEM (Figure S7). It can be seen that the morphology of MoP@C is almost unchanged. The MoP nanoparticles uniformly disperse in the carbon matrix without aggregation, indicating the structural stability of the MoP@C composite. These results are clear evidence that the urchin-like

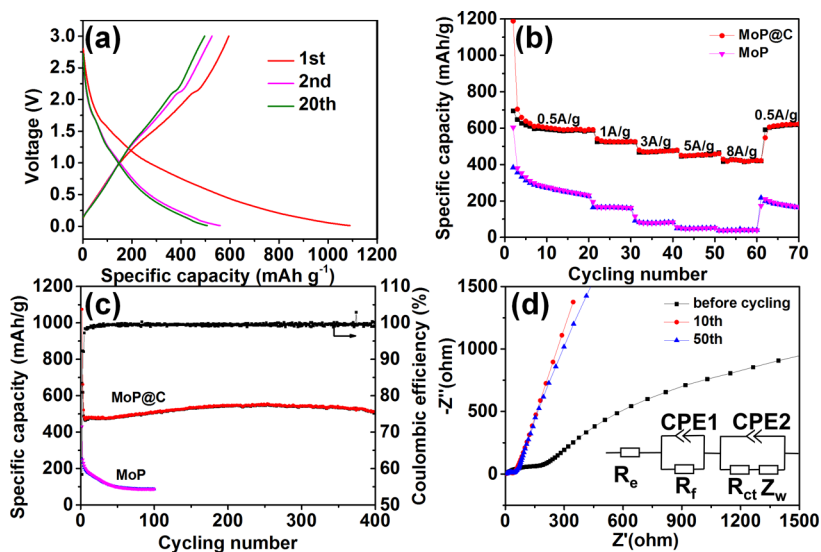


Figure 4. Electrochemical properties of the MoP: (a) galvanostatic charge/discharge profiles, (b) rate capabilities of MoP@C and MoP, (c) cycling performance of the MoP@C and MoP electrode at 1 A g^{-1} , and (d) EIS Nyquist plots of the MoP@C electrode (inset: equivalent circuit model).

MoP@C electrode exhibits superior structure stability and electrochemical reversibility.

Electrochemical impedance spectroscopy (EIS) was performed to investigate the kinetic properties of the electrode. The urchin-like MoP@C electrodes were analyzed before cycling and after 10 and 50 cycles at 500 mA g^{-1} as shown in Figure 4d. All Nyquist plots exhibit an identical feature with a straight sloping line on the low frequency region and a superimposed semicircle on the medium frequency region. The measured impedance spectra are fitted by an equivalent circuit model (Figure S8), and the corresponding fitting parameters are shown in Table S1. It is evident that the charge-transfer resistance (R_{ct}) of the electrode decreases from 182 to $31\ \Omega$ after cycling, which in general is observed in other anode materials²¹ and ascribed to a superior active contact after cycling.^{21,45} The Warburg impedance (Z_w) is related to the solid diffusion of Li^+ . After 10 cycles, the Z_w remains almost unchanged between 10 and 50 cycles. Similar to Z_w , the R_e and R_{ct} values of the electrode have no obvious changes between 10 and 50 cycles, indicating that electrode is stable after 10 cycles. These results further confirm the integrity of the urchin-like MoP@C and the stability of the SEI film on the anode surface, which matched well with the superior electrochemical performance.

Cyclic voltammetry (CV) was used to analyze the lithium storage mechanism of the urchin-like MoP@C electrode. The CV curves at 0.2 mV s^{-1} in the voltage window of 0.01–3 V are illustrated in Figure 5a. The cathodic curve in the first cycle is significantly different from the subsequent cycles, which presents a distinct peak at around 0.6 V corresponding to the SEI film formation on the electrode surface.⁴⁶ After the first cycle, this peak disappears and the curves almost overlap for subsequent cycles without significant peak shift, indicating an excellent reversibility of the MoP@C electrode. During the cathodic scan peaks at 1.7, 1.13, and 0.24 V can be attributed to the continuous intercalation of Li^+ into the MoP to form Li_xMoP and the reduction of Li_xMoP into metallic Mo and Li_3P ,^{46–48} respectively, which is consistent with the charge/discharge profiles. During the anodic process, peaks at 0.32, 1.5, and 2.03 V could be explained by the Li^+ extraction from

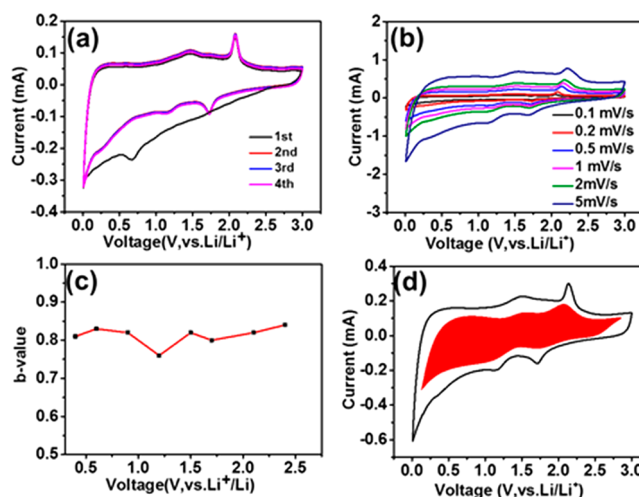
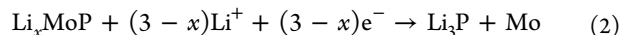


Figure 5. (a) CV curves at 0.2 mV s^{-1} , (b) CV curves of electrode at different sweep rates, (c) b -values at different voltage (0.5 mV s^{-1}), and (d) contribution of capacitive current (shaded region) at the scan rate of 0.5 mV s^{-1} .

the bulk materials. Therefore, the lithiation process could be expressed as follows:



The capacitive effect was explored via CV curves at sweep rates from 0.1 to 5 mV s^{-1} . The corresponding results are shown in Figure 5b. The total charge storage in the electrode materials can be separated into three mechanisms: the faradaic contribution from the Li^+ insertion, the surface pseudocapacitance from the charge transfer process at the electrode surface and the nonfaradaic contribution from the electrical double-layer effects. The contribution from diffusion and capacitive processes can be estimated according to the relationship^{45,49,50}

$$i = av^b \quad (3)$$

where a and b are adjustable parameters. The b value could be obtained from the slope of the log i versus log v . The b value varies from 0.5 (diffusion-controlled process) to 1 (capacitive process). The b -value is calculated for the anodic process. From Figure 5c, at the anodic peak the b value is 0.72, which suggests the mixed contribution for the charge storage. At other potentials, the b values are larger than 0.8, indicating that the process is controlled by the capacitive behavior. Moreover, the contribution from the diffusion and the capacitive processes could be quantitatively determined through equation⁴⁵

$$i(v) = k_1v + k_2v^{1/2} \quad (4)$$

As illustrated in Figure 5d, 56% of the charge storage is from the surface capacitive processes, which helps to explain the high rate performance.

3. CONCLUSION

In conclusion, the urchin-like MoP@C nanocomposite is synthesized by a fast and scalable method, in which ultrasmall MoP nanocrystals are uniformly dispersed in carbon matrix. Such a unique structure is beneficial as it could refrain the MoP nanocrystals from aggregation as well as provide more direct contact between MoP and the elastic carbon matrix. Such hierarchical nanoarchitecture helps to relieve the stress due to volume changes upon cycling and to avoid detrimental reactions between MoP and the electrolyte. These merits contribute to the enhanced electrochemical performances of MoP@C composite electrode in LIBs. It delivers a high specific capacity of 378 mAh g⁻¹ after 400 cycles at 1A g⁻¹ and exhibits excellent rate capability, as well as good cycling stability.

■ ASSOCIATED CONTENT

Supporting Information

The Supporting Information is available free of charge on the ACS Publications website at DOI: 10.1021/acsam.8b01580.

Experimental section, elemental mapping of MoP@C, SEM images of MoP particles without dopamine, XPS survey spectrum of MoP@C, and equivalent circuit model used for fitting (PDF)

■ AUTHOR INFORMATION

Corresponding Authors

*E-mail: clairexiong@boisestate.edu.

*E-mail: liaoxyz@sjtu.edu.cn.

ORCID

Hui Xiong: 0000-0003-3126-1476

Notes

The authors declare no competing financial interest.

■ ACKNOWLEDGMENTS

The authors acknowledge supports by Micron School of Materials Science and Engineering at Boise State University and the National Natural Science Foundation of China (21336003, 21676165), the National Basic Research Program of China (2014CB239700), and the Shanghai Natural Science Foundation (15ZR1422300).

■ REFERENCES

- (1) Yoo, E.; Kim, J.; Hosono, E.; Zhou, H.; Kudo, T.; Honma, I. Large Reversible Li Storage Of Graphene Nanosheet Families For Use In Rechargeable Lithium Ion Batteries. *Nano Lett.* **2008**, *8*, 2277–2282.
- (2) Nam, K. T. Virus-Enabled Synthesis And Assembly Of Nanowires For Lithium Ion Battery Electrodes. *Science* **2006**, *312*, 885–888.
- (3) Oumellal, Y.; Rougier, A.; Nazri, G. A.; Tarascon, J. M.; Aymard, L. Metal Hydrides For Lithium-Ion Batteries. *Nat. Mater.* **2008**, *7*, 916–921.
- (4) Armand, M.; Tarascon, J. M. Building Better Batteries. *Nature* **2008**, *451*, 652–657.
- (5) Chen, G.; Zhou, M.; Catanach, J.; Liaw, T.; Fei, L.; Deng, S. G.; Luo, H. M. Solvothermal Route Based In Situ Carbonization To Fe₃O₄@C As Anode Material For Lithium Ion Battery. *Nano Energy* **2014**, *8*, 126–132.
- (6) Salián, G. D.; Koo, B. M.; Lefevre, C.; Cottineau, T.; Lebouin, C.; Tesfaye, A. T.; Knauth, P.; Keller, V.; Djenizian, T. Niobium Alloying of Self-Organized TiO₂ Nanotubes as an Anode for Lithium-Ion Microbatteries. *Adv. Mater. Technol-Us* **2018**, *3*, 1700274.
- (7) Shao, Q. G.; Tang, J. E.; Sun, Y. G.; Li, J.; Zhang, K.; Yuan, J. S.; Zhu, D. M.; Qin, L. C. Unique Interconnected Graphene/SnO₂ Nanoparticle Spherical Multilayers For Lithium-Ion Battery Applications. *Nanoscale* **2017**, *9*, 4439–4444.
- (8) Ma, T. Y.; Yu, X. N.; Li, H. Y.; Zhang, W. G.; Cheng, X. L.; Zhu, W. T.; Qiu, X. P. High Volumetric Capacity of Hollow Structured SnO₂@Si Nanospheres for Lithium-Ion Batteries. *Nano Lett.* **2017**, *17*, 3959–3964.
- (9) Fan, X. L.; Zhu, Y. J.; Luo, C.; Gao, T.; Suo, L. M.; Liou, S. C.; Xu, K.; Wang, C. S. In Situ Lithiated Fe₃/C Nanocomposite As High Energy Conversion-Reaction Cathode For Lithium-Ion Batteries. *J. Power Sources* **2016**, *307*, 435–442.
- (10) Li, Y.; Yao, F. N.; Cao, Y.; Yang, H. Y.; Feng, Y. Y.; Feng, W. The Mediated Synthesis Of Fe₃ Nanocrystals Through (NH₄)₃(Fef₆) Precursors As The Cathode Material For High Power Lithium Ion Batteries. *Electrochim. Acta* **2017**, *253*, 545–553.
- (11) Rui, K.; Wen, Z. Y.; Lu, Y.; Jin, J.; Shen, C. One-Step Solvothermal Synthesis Of Nanostructured Manganese Fluoride As An Anode For Rechargeable Lithium-Ion Batteries And Insights Into The Conversion Mechanism. *Adv. Energy Mater.* **2015**, *5*, 1401716.
- (12) Zhu, C. B.; Kopold, P.; Li, W. H.; van Aken, P. A.; Maier, J.; Yu, Y. A General Strategy to Fabricate Carbon-Coated 3D Porous Interconnected Metal Sulfides: Case Study of SnS/C Nanocomposite for High-Performance Lithium and Sodium Ion Batteries. *Adv. Sci.* **2015**, *2*, 1500200.
- (13) Teng, Y. Q.; Zhao, H. L.; Zhang, Z. J.; Li, Z. L.; Xia, Q.; Zhang, Y.; Zhao, L. N.; Du, X. F.; Du, Z. H.; Lv, P. P.; Swierczek, K. MoS₂ Nanosheets Vertically Grown on Graphene Sheets for Lithium-Ion Battery Anodes. *ACS Nano* **2016**, *10*, 8526–8535.
- (14) Xu, Y. X.; Li, W. Y.; Zhang, F.; Zhang, X. L.; Zhang, W. J.; Lee, C. S.; Tang, Y. B. In Situ Incorporation Of Fes Nanoparticles/Carbon Nanosheets Composite With An Interconnected Porous Structure As A High-Performance Anode For Lithium Ion Batteries. *J. Mater. Chem. A* **2016**, *4*, 3697–3703.
- (15) Li, Z. Y.; Zhang, J. C.; Gao, R.; Zhang, H.; Zheng, L. R.; Hu, Z. B.; Liu, X. F. Li-Substituted Co-Free Layered P₂/O₃ Biphasic Na_{0.67}Mn_{0.55}Ni_{0.25}Ti_{0.2-x}LixO₂ as High-Rate-Capability Cathode Materials for Sodium Ion Batteries. *J. Phys. Chem. C* **2016**, *120*, 9007–9016.
- (16) Wu, J. J.; Fu, Z. W. Pulsed-Laser-Deposited Sn4P3 Electrodes for Lithium-Ion Batteries. *J. Electrochem. Soc.* **2009**, *156*, A22–A26.
- (17) Wang, X. J.; Chen, K.; Wang, G.; Liu, X. J.; Wang, H. Rational Design of Three-Dimensional Graphene Encapsulated with Hollow FeP@Carbon Nanocomposite as Outstanding Anode Material for Lithium Ion and Sodium Ion Batteries. *ACS Nano* **2017**, *11*, 11602–11616.
- (18) Jiang, J.; Wang, C. D.; Li, W.; Yang, Q. One-Pot Synthesis Of Carbon-Coated NiSP4 Nanoparticles And Cop Nanorods For High-

Rate And High-Stability Lithium-Ion Batteries. *J. Mater. Chem. A* **2015**, *3*, 23345–23351.

(19) Mao, J.; Fan, X.; Luo, C.; Wang, C. Building Self-Healing Alloy Architecture for Stable Sodium-Ion Battery Anodes: A Case Study of Tin Anode Materials. *ACS Appl. Mater. Interfaces* **2016**, *8*, 7147–7155.

(20) Fan, X.; Mao, J.; Zhu, Y.; Luo, C.; Suo, L.; Gao, T.; Han, F.; Liou, S. C.; Wang, C. Superior Stable Self-Healing SnP₃ Anode for Sodium-Ion Batteries. *Adv. Energy Mater.* **2015**, *5*, 1500174.

(21) Han, F.; Zhang, C. Z.; Yang, J. X.; Ma, G. Z.; He, K. J.; Li, X. K. Well-Dispersed And Porous FeP@C Nanoplates With Stable And Ultrafast Lithium Storage Performance Through Conversion Reaction Mechanism. *J. Mater. Chem. A* **2016**, *4*, 12781–12789.

(22) Wu, C.; Kopold, P.; van Aken, P. A.; Maier, J.; Yu, Y. High Performance Graphene/Ni₂P Hybrid Anodes for Lithium and Sodium Storage through 3D Yolk-Shell-Like Nanostructural Design. *Adv. Mater.* **2017**, *29*, 1604015.

(23) Zhao, F. P.; Han, N.; Huang, W. J.; Li, J. J.; Ye, H. L.; Chen, F. J.; Li, Y. G. Nanostructured Cup₂/C Composites As High-performance Anode Materials For Sodium Ion Batteries. *J. Mater. Chem. A* **2015**, *3*, 21754–21759.

(24) Li, Q.; Ma, J. J.; Wang, H. J.; Yang, X.; Yuan, R.; Chai, Y. Q. Interconnected Ni₂P Nanorods Grown On Nickel Foam For Binder Free Lithium Ion Batteries. *Electrochim. Acta* **2016**, *213*, 201–206.

(25) Han, Z.; Wang, B. B.; Liu, X. J.; Wang, G.; Wang, H.; Bai, J. T. Peapod-Like One-Dimensional (1D) Cop Hollow Nanorods Embedded Into Graphene Networks As An Anode Material For Lithium-Ion Batteries. *J. Mater. Sci.* **2018**, *53*, 8445–8459.

(26) Lu, Y.; Tu, J. P.; Xiong, Q. Q.; Qiao, Y. Q.; Wang, X. L.; Gu, C. D.; Mao, S. X. Synthesis Of Dinickel Phosphide (Ni₂P) For Fast Lithium-Ion Transportation: A New Class Of Nanowires With Exceptionally Improved Electrochemical Performance As A Negative Electrode. *RSC Adv.* **2012**, *2*, 3430–3436.

(27) McEnaney, J. M.; Crompton, J. C.; Callejas, J. F.; Popczun, E. J.; Biacchi, A. J.; Lewis, N. S.; Schaak, R. E. Amorphous Molybdenum Phosphide Nanoparticles for Electrocatalytic Hydrogen Evolution. *Chem. Mater.* **2014**, *26*, 4826–4831.

(28) Han, S.; Feng, Y. L.; Zhang, F.; Yang, C. Q.; Yao, Z. Q.; Zhao, W. X.; Qiu, F.; Yang, L. Y.; Yao, Y. F.; Zhuang, X. D.; Feng, X. L. Metal-Phosphide-Containing Porous Carbons Derived from an Ionic-Polymer Framework and Applied as Highly Efficient Electrochemical Catalysts for Water Splitting. *Adv. Funct. Mater.* **2015**, *25*, 3899–3906.

(29) Xiao, P.; Sk, M. A.; Thia, L.; Ge, X. M.; Lim, R. J.; Wang, J. Y.; Lim, K. H.; Wang, X. Molybdenum Phosphide As An Efficient Electrocatalyst For The Hydrogen Evolution Reaction. *Energy Environ. Sci.* **2014**, *7*, 2624–2629.

(30) Yang, Y.; Luo, M.; Xing, Y.; Wang, S.; Zhang, W.; Lv, F.; Li, Y.; Zhang, Y.; Wang, W.; Guo, S. A Universal Strategy for Intimately Coupled Carbon Nanosheets/MoM Nanocrystals (M = P, S, C, and O) Hierarchical Hollow Nanospheres for Hydrogen Evolution Catalysis and Sodium-Ion Storage. *Adv. Mater.* **2018**, *30*, 1706085.

(31) Kim, M. G.; Lee, S.; Cho, J. Highly Reversible Li-Ion Intercalating MoP₂ Nanoparticle Cluster Anode for Lithium Rechargeable Batteries. *J. Electrochem. Soc.* **2009**, *156*, A89–A94.

(32) Li, G. H.; Yang, H.; Li, F. C.; Du, J.; Shi, W.; Cheng, P. Facile Formation Of A Nanostructured Nip₂@C Material For Advanced Lithium-Ion Battery Anode Using Adsorption Property Of Metal-Organic Framework. *J. Mater. Chem. A* **2016**, *4*, 9593–9599.

(33) Chen, J.; Xia, X. H.; Tu, J. P.; Xiong, Q. Q.; Yu, Y. X.; Wang, X. L.; Gu, C. D. Co₃O₄-C Core-Shell Nanowire Array As An Advanced Anode Material For Lithium Ion Batteries. *J. Mater. Chem.* **2012**, *22*, 15056–15061.

(34) Chen, Y.-Y.; Zhang, Y.; Jiang, W.-J.; Zhang, X.; Dai, Z.; Wan, L.-J.; Hu, J.-S. Pomegranate-like N,P-Doped Mo₂C@C Nanospheres as Highly Active Electrocatalysts for Alkaline Hydrogen Evolution. *ACS Nano* **2016**, *10*, 8851–8860.

(35) Scherrer, P. *Bestimmung der inneren Struktur und der Größe von Kolloidteilchen mittels Röntgenstrahlen*; Springer: Berlin, 1912; pp 387–409.

(36) Zhao, C. T.; Yu, C.; Qiu, B.; Zhou, S.; Zhang, M. D.; Huang, H. W.; Wang, B. Q.; Zhao, J. J.; Sun, X. L.; Qiu, J. S. Ultrahigh Rate and Long-Life Sodium-Ion Batteries Enabled by Engineered Surface and Near-Surface Reactions. *Adv. Mater.* **2018**, *30*, 1702486.

(37) Huang, Z. D.; Hou, H. S.; Wang, C.; Li, S. M.; Zhang, Y.; Ji, X. B. Molybdenum Phosphide: A Conversion-type Anode for Ultralong-Life Sodium-Ion Batteries. *Chem. Mater.* **2017**, *29*, 7313–7322.

(38) Chen, J. J.; Mao, Z. Y.; Zhang, L. X.; Wang, D. J.; Xu, R.; Bie, L. J.; Fahlman, B. D. Nitrogen-Deficient Graphitic Carbon Nitride with Enhanced Performance for Lithium Ion Battery Anodes. *ACS Nano* **2017**, *11*, 12650–12657.

(39) Guan, J.; Zhong, X. W.; Chen, X.; Zhu, X. J.; Li, P. L.; Wu, J. H.; Lu, Y. L.; Yu, Y.; Yang, S. F. Expanding Pore Sizes Of Zif-8-Derived Nitrogen-Doped Microporous Carbon Via C-60 Embedding: Toward Improved Anode Performance For The Lithium-Ion Battery. *Nanoscale* **2018**, *10*, 2473–2480.

(40) Gu, X.; Yue, J.; Chen, L.; Liu, S.; Xu, H. Y.; Yang, J.; Qian, Y. T.; Zhao, X. B. Coaxial MnO/N-Doped Carbon Nanorods For Advanced Lithium-Ion Battery Anodes. *J. Mater. Chem. A* **2015**, *3*, 1037–1041.

(41) Chen, Y. C.; Hung, T. F.; Hu, C. W.; Chiang, C. Y.; Huang, C. W.; Su, H. C.; Liu, R. S.; Lee, C. H.; Chang, C. C. Rutile-Type (Ti,Sn)O₂ Nanorods As Efficient Anode Materials Toward Its Lithium Storage Capabilities. *Nanoscale* **2013**, *5*, 2254–2258.

(42) Chang, K.; Geng, D. S.; Li, X. F.; Yang, J. L.; Tang, Y. J.; Cai, M.; Li, R. Y.; Sun, X. L. Ultrathin MoS₂/Nitrogen-Doped Graphene Nanosheets with Highly Reversible Lithium Storage. *Adv. Energy Mater.* **2013**, *3*, 839–844.

(43) Xu, B. H.; Guan, X. G.; Zhang, L. Y.; Liu, X. W.; Jiao, Z. B.; Liu, X. H.; Hu, X. Q.; Zhao, X. S. A Simple Route To Preparing Gamma-Fe₂O₃/RGO Composite Electrode Materials For Lithium Ion Batteries. *J. Mater. Chem. A* **2018**, *6*, 4048–4054.

(44) Cao, J. Y.; Zhu, Z. T.; Xu, J.; Tao, M.; Chen, Z. D. Nitrogen-Doped Porous Graphene As A Highly Efficient Cathodic Electrocatalyst For Aqueous Organic Redox Flow Battery Application. *J. Mater. Chem. A* **2017**, *5*, 7944–7951.

(45) Wang, J.; Polleux, J.; Lim, J.; Dunn, B. Pseudocapacitive Contributions To Electrochemical Energy Storage In TiO₂ (Anatase) Nanoparticles. *J. Phys. Chem. C* **2007**, *111*, 14925–14931.

(46) Wang, X.; Sun, P. P.; Qin, J. W.; Wang, J. Q.; Xiao, Y.; Cao, M. H. A Three-Dimensional Porous Mop@C Hybrid As A High-Capacity, Long-Cycle Life Anode Material For Lithium-Ion Batteries. *Nanoscale* **2016**, *8*, 10330–10338.

(47) Von Lim, Y.; Huang, S.; Zhang, Y.; Kong, D.; Wang, Y.; Guo, L.; Zhang, J.; Shi, Y.; Chen, T. P.; Ang, L. K.; Yang, H. Y. Bifunctional Porous Iron Phosphide/Carbon Nanostructure Enabled High-Performance Sodium-Ion Battery And Hydrogen Evolution Reaction. *Energy Storage Materials* **2018**, *15*, 98–107.

(48) Xu, Z.; Zeng, Y.; Wang, L.; Li, N.; Chen, C.; Li, C.; Li, J.; Lv, H.; Kuang, L.; Tian, X. Nanoconfined Phosphorus Film Coating On Interconnected Carbon Nanotubes As Ultrastable Anodes For Lithium Ion Batteries. *J. Power Sources* **2017**, *356*, 18–26.

(49) Chao, D. L.; Zhu, C. R.; Yang, P. H.; Xia, X. H.; Liu, J. L.; Wang, J.; Fan, X. F.; Savilov, S. V.; Lin, J. Y.; Fan, H. J.; Shen, Z. X. Array Of Nanosheets Render Ultrafast And High-Capacity Na-Ion Storage By Tunable Pseudocapacitance. *Nat. Commun.* **2016**, *7*, 12122.

(50) Chen, C. J.; Wen, Y. W.; Hu, X. L.; Ji, X. L.; Yan, M. Y.; Mai, L. Q.; Hu, P.; Shan, B.; Huang, Y. H. Na⁺ Intercalation Pseudocapacitance In Graphene-Coupled Titanium Oxide Enabling Ultra-Fast Sodium Storage And Long-Term Cycling. *Nat. Commun.* **2015**, *6*, 6929.